

Modal Analysis of Instabilities in the BoLT-2 Flowfield

Zachary M. Johnston*, Maziar S. Hemati†, and Graham V. Candler‡

Department of Aerospace Engineering and Mechanics, University of Minnesota, Minneapolis, MN 55455

Boundary layer disturbances in the Boundary Layer Turbulence (BoLT-2) flowfield are investigated using a combination of low-dissipation numerics and a novel shock capturing scheme. This allows us to investigate the later stages of the transition process governed by nonlinear evolution of the boundary layer state. Unsteady simulations using US3D are performed with broadband stochastic forcing to mimic quiet wind tunnel noise. Disturbances are introduced at an interpolated inflow plane located downstream of the leading edge to allow disturbances to grow which are induced by boundary layer instability mechanisms. Two-dimensional time series snapshots are collected at streamwise locations along the geometry to compute spatio-temporal information from extracted boundary layer modes. Modal analysis is performed with a streaming version of total dynamic mode decomposition (STDMD) with a compressible energy norm weighting to identify modes associated with distinct transition processes. Frequencies computed from STDMD modes show excellent agreement with power spectral density peaks measured from experiments and simulation.

I. Introduction

Laminar to turbulent boundary layer transition results in significantly higher aerodynamic heating and skin friction. For high speed applications, a given flight trajectory a vehicle operates in typically dictates the thermal loading of the vehicle. Therefore, knowing when and where flow transition occurs on a vehicle is helpful for the optimization of its thermal protection system. More importantly, understanding the relevant physics leading up to the nonlinear transition regime of hypersonic boundary layers is not well characterized.

The prediction of transition in hypersonic boundary layers typically involves a form of boundary layer stability analysis. For two-dimensional flows and axi-symmetric geometries, modal stability analysis techniques have been used to accurately predict early onset of transition for cone configurations [1, 2]. This has proven useful for understanding a single dominant instability mechanism that can contribute to transition by computing growth rates. However, three-dimensional boundary layers can contain multiple instabilities causing amplification of disturbance quantities and potentially coalesce. Therefore, the presence of multiple instabilities makes it difficult to accurately predict transition for complex geometries or for realistic flight deviations (i.e., dispersion in angle of attack). This is important for understanding transition prediction since there is uncertainty with how multiple three-dimensional transition mechanisms can interact leading to turbulence.

The Boundary-Layer Transition (BoLT) flight experiment has proven to be successful in testing and developing stability analysis tools using numerical simulation [3, 4] and comparisons are consistent with experimental ground test measurements [5, 6]. Therefore, the Boundary Layer Turbulence (BoLT-2) flight experiment is the next upcoming hypersonic flight experiment. The purpose of the sounding rocket flight test is to collect measurements to characterize boundary layer transition to turbulence at hypersonic flow conditions for the BoLT shape. This provides opportunities to further test, develop, and verify stability analysis tools through boundary layer breakdown using state-of-the-art computational analyses and ground tests to study transition to turbulence in flight. The geometry contains four swept edges that are meant to isolate regions for individual research studies on BoLT-2 including natural transition on the primary (top) surface and boundary layer trips on the secondary (bottom) surface [7]. The goal of this paper is to provide insight of the natural transition process through the nonlinear transition regime using a modal analysis tool that is consistent with the computational methodology.

The scope of this paper is to identify which mode(s) are dominant and are contributing the most to the underlying flow dynamics in regions experiencing nonlinear disturbance amplification at subscale wind tunnel conditions. High-fidelity simulations of the Navier-Stokes equations are computed for Mach 6 flow conditions over a 25% scaled model of a 1.477m length BoLT-2 configuration. Stochastic forcing is applied to the pressure field by satisfying the acoustic-mode to

*Graduate Research Assistant, AIAA Student Member

†Associate Professor, AIAA Associate Fellow

‡McKnight Presidential Chair, Distinguished McKnight and Russell J. Penrose Professor, AIAA Fellow

excite instabilities and allowing the boundary layer to naturally select growth of introduced disturbances. Spatio-temporal information is computed from the forced DNS data using a streaming version of total dynamic mode decomposition (STDMD) with an energy norm weighting to quantify modes associated with boundary layer transition processes. Power spectral densities computed from surface pressure measurements taken in the Mach 6 quiet tunnel (M6QT) at Texas A&M University show excellent agreement with the dominant mode identified to be the primary source of nonlinear disturbance growth causing breakdown.

A. Instabilities in Three-Dimensional Hypersonic Boundary Layers

Several types of instabilities can contribute to transition by means of amplifying disturbances quantities leading to transition within a hypersonic boundary layer. Using linear stability theory (LST), two types of instability mechanisms were identified by Mack in two-dimensional boundary layers and termed first- and second-modes [8]. The first- and second-modes can become important to the transition process by absorbing energy from the flowfield and have been observed in experiments and simulations. The first mode is a viscous instability similar to Tollmien-Schlichting waves as seen in incompressible flow. The second mode is an inviscid instability where the boundary layer acts as an acoustic wave guide such that the instability is tuned to the local boundary layer properties causing a reflection of acoustic waves between the wall and the relative sonic line [9]. For hypersonic flows, the second-mode is typically found to be more unstable over first-mode in highly compressible boundary layers [9]. Previous work by Li et al. [10] has shown for high-speed boundary layer flows that three-dimensional secondary instabilities can arise and lead to nonlinear evolution of second-mode waves for cone configurations.

With the extension to three-dimensional space, additional transition mechanisms can exist within a compressible boundary layer. One of these instabilities is the so called crossflow instability. This is produced by a crossflow velocity component when the boundary layer velocity profile contains an inflection point caused by misalignment of the inviscid velocity vector and spanwise pressure gradient due to varying momentum and pressure gradients near the wall. The inflection point can become inviscidly unstable leading to transition and has two types of modes. One type is a stationary mode resulting from steady forcing that produces an inflection point taking the form of stationary crossflow vortices [11]. For BoLT, Thome et al. [3] showed the stationary crossflow mode can become a dominant transition mechanism due to its sensitivity to roughness. The second type is a traveling mode with an associated wave angle and phase speed. Both modes have been observed for a number of configurations in the past such as for a cone at an angle of attack [12], a yawed cone [13], the HIFiRE-5 2:1 elliptic cone [11], and BoLT [4].

B. Modal Analysis Applied to BoLT

Many types of modal analysis techniques have been used to extract spatio-temporal information from flowfield snapshots generated by simulations. An overview of current modal analysis techniques with their applications are described in the papers by Taira et al. [14, 15]. Many of these analysis techniques are purely data-driven and typically apply modal decomposition to a dataset of a particular flow variable, or of an operator relevant to the system. One such modal analysis tool capable of extracting pertinent information from computational datasets is dynamic mode decomposition (DMD). DMD is a modal analysis tool that can extract dynamical information provided a sequence of snapshots in time.

Numerical simulations and analysis by Knutson et al. [4] using Sparsity-promoting DMD (SPDMD) [16] revealed multiple instabilities in the BoLT flowfield. These instabilities have been defined as a vortical mode near the centerline, traveling crossflow near the swept edge, and a region containing mixed modes. This has provided useful insight into the types of transition mechanisms contributing to linear growth of disturbances for BoLT and are consistent with subscale experimental measurements. At higher Reynolds numbers, there is a development of stationary crossflow vortices located between the centerline and swept edge. The interaction of inviscid disturbances with the crossflow vortices have been shown to initiate breakdown observed on the surface of past BoLT-2 simulations [17].

Analysis using nonlinear parabolic stability equations (NPSE) by Mullen and Reed [18] have predicted N-factors of the BoLT-2 subscale geometry to reach over 10 for both second-mode and traveling crossflow towards the end of the geometry. Therefore, this provides estimates regarding maximum relative amplitudes at a particular region and for a single instability mechanism. Since multiple instability mechanisms are present Direct Numerical Simulation (DNS) is chosen as the tool to simulate linear and nonlinear flow processes making it possible to study potential mode interaction and secondary flow effects. Current work seeks to apply off surface modal analysis to reveal boundary layer modes contributing to breakdown by following forced DNS methodology. The modal analysis approach is consistent with the computational methodology to extract pertinent information from the forced DNS dataset.

C. Forcing Inputs and Numerical Method

In flight and wind tunnel experiments, boundary layer instabilities arise due to some type of external forcing that takes form of freestream disturbances that enter the boundary layer through the process known as receptivity. Much progress has been made to more accurately characterize the disturbance environment in flight [19] and this continues to be an area of further research. In hypersonic wind tunnels, a boundary layer develops on the nozzle wall which can radiate acoustic noise and become significant if the boundary layer becomes turbulent. Therefore, hypersonic "quiet" wind tunnels ensure the nozzle wall boundary layer remains laminar using techniques such as polishing the nozzle wall and introducing bleed slots. Since comparisons are being made to wind tunnel measurements, the random forcing approach in this paper is based on the approach first introduced by Hader and Fasel [20] and is meant to mimic effects similar to quiet wind tunnel noise. This provides a more representative model of a quiet wind tunnel environment by using a broadband forcing function allowing the boundary layer to select a response representative of natural transition. This is different than what was previously used to investigate boundary layer instabilities on BoLT by Knutson et al. [4] which applied a strip of stochastic momentum forcing at the wall. DNS is used as a numerical tool for boundary layer analysis to simulate the evolution of the boundary layer state. A high-order, low-dissipation numerical method [21] is used and is required to accurately capturing boundary layer instabilities. This method is sensitive to flow discontinuities (i.e., shock waves) and therefore a custom "shock sensor" is used to tailor a dissipative flux to maintain numerical stability in regions as needed.

The remainder of the paper is organized as follows. Section II describes the computational methodology, including how disturbances are introduced into the flowfield. The results are summarized and compared to experiments in Section III by first showing the steady flowfield and qualitative surface heating comparison motivating the current work. Section IV shows the boundary layer response of the proposed forcing approach with qualitative identification of vortex structures supporting disturbance energy growth. Sections V proposes the modal analysis methodology for identifying dominant boundary layer modes. Lastly, the modal analysis results are introduced and discussed.

II. Computational Methodology

A. Numerical Scheme

The simulations performed in this paper solve the compressible Navier-Stokes equations for a perfect gas in conservation form,

$$\frac{\partial U}{\partial t} + \frac{\partial F_j}{\partial x_j} = \frac{\partial F_j^v}{\partial x_j} \quad (1)$$

The vector of conservative variables, convective fluxes, and viscous fluxes are represented respectively by,

$$U = \begin{Bmatrix} \rho \\ \rho u_i \\ E \end{Bmatrix}, \quad F_j = \begin{Bmatrix} \rho u_j \\ \rho u_i u_j + p \delta_{ij} \\ (E + p)u_j \end{Bmatrix}, \quad F_j^v = \begin{Bmatrix} 0 \\ \sigma_{ij} \\ \sigma_{ij}u_i - q_j \end{Bmatrix}. \quad (2)$$

All computations assume a perfect gas based on the low freestream enthalpy with the equation of state for an ideal gas,

$$p = \rho RT. \quad (3)$$

The total energy per unit volume takes into account kinetic and internal energies,

$$E = \frac{1}{2}\rho u_i u_i + \rho c_v T. \quad (4)$$

The viscous stress tensor is defined as,

$$\sigma_{ij} = \mu \left(\frac{\partial u_i}{\partial x_j} + \frac{\partial u_j}{\partial x_i} \right) - \lambda \frac{\partial u_k}{\partial x_k} \delta_{ij}, \quad (5)$$

where μ is the dynamic viscosity and we employ Stokes' assumption of zero bulk viscosity to obtain $\lambda = -\frac{2}{3}\mu$. Sutherlands Law is used to account for the effect of temperature on viscosity using $\mu_o = 1.458 \times 10^{-6}$ kg/m-s and $T_o = 110.3K$,

$$\mu(T) = \mu_o \frac{T^{3/2}}{T + T_o}. \quad (6)$$

The heat flux vector is derived from Fourier’s Law of heat conduction and related by the thermal gradient,

$$q_j = -\kappa \frac{\partial T}{\partial x_j}, \quad (7)$$

where the thermal conductivity, $\kappa = \mu c_p / Pr$, uses a constant Prandtl number of 0.72 and the ratio of specific heats as $\gamma = 1.4$.

The governing equations were solved in compact conservative form using a finite volume formulation [22] and using a compact-gradient scheme [23] for the spatial discretization of the convective flux evaluation. All simulations evaluate the convective flux by reconstructing variables at each face for the symmetric flux using a fourth order gradient based interpolation,

$$\phi_{i+1/2} = \frac{(\phi_i + \phi_{i+1})}{2} + \frac{(\delta\phi_i + \delta\phi_{i+1})}{3}, \quad (8)$$

where $\delta\phi_i$ corresponds to the dot product of the gradient of ϕ in cell i and the vector from the cell center of i to the face center of $i + 1/2$. The viscous fluxes are computed using a second order central scheme. The low dissipation inviscid fluxes are split into a non-dissipative central component and a dissipative component. The non-dissipative central component is used for the primary flux evaluation and applying a small portion of the dissipative component taking the following form,

$$\mathbf{F} = \mathbf{F}_{central} + \alpha \mathbf{F}_{diss}. \quad (9)$$

The dissipative flux, \mathbf{F}_{diss} , uses the dissipative portion of an upwind-biased TVD scheme based on flux vector splitting [24] with a MUSCL reconstruction for second order accuracy [25]. The dissipative component of this scheme is made up of the dissipative flux based on a scalar, $\alpha \in [0, 1]$, to minimize the percentage of the dissipative flux added. The purpose of this is to selectively add dissipation in regions that require it to maintain numerical stability by setting a range for α . The shock sensor is similar to the shock-capturing scheme described by Larsson et al. [26] with a slight modification [17]. For this particular problem, the dissipation factor needed to be modified to increase α in the azimuthal direction past the swept edge to avoid unwanted spurious behavior when introducing disturbances. Without accounting for this numerical instability could lead to contamination of extracted data. Also, the shock sensor tailors a slight increase in dissipation to the region experiencing breakdown to maintain numerical stability. Numerical instability was observed when using the low dissipation numerics originating from disturbances experiencing nonlinear growth. This required a minimum value of $\alpha = 0.05$ to be set globally additionally helping baseflow convergence. A value higher than $\alpha = 0.1$ significantly attenuates propagating wave amplitudes as a result of the confined streamwise grid spacing.

Implicit time integration is used to overcome the restrictive stable time step limitations imposed by explicit methods. Implicit time integration is achieved by linearizing the fluxes in time and approximately solving the resulting linear system of equations using Data-Parallel Line Relaxation (DPLR) [27] for steady state simulations. For the unsteady simulations, a time accurate implicit method is necessary. In the present work, we use the second-order backward differentiation formula (BDF2) with Newton’s method to solve the nonlinear equations [28]. At each Newton subiteration, the linear system is solved using DPLR. Without higher-order time integration, boundary layer instabilities are severely attenuated due to the numerical dissipation associated with first-order methods [28]. Previous work by Knutson also showed 80 timesteps per period sufficiently captures second-mode disturbance growth for a 7 degree straight cone using BDF2 time integration. In present work, a constant timestep of $20 \times 10^{-9}s$ is used for the unsteady simulations corresponding to 100 timesteps per period for a 500kHz wave. Scaling of second-mode based on Stetson [29] of the baseflow state predicts the highest second-mode frequency to reach 480kHz. The chosen timestep corresponds to a global Courant-Friedrichs-Lewy (CFL) number of 11 dictated by the first cell off the wall and a local CFL number of less than one in the region of interest.

B. Boundary Conditions

All simulations use a zonal DNS approach by splitting the computational domain and applying forcing to the downstream subdomain. Therefore, this requires an inflow interpolation approach thereby neglecting the receptivity process, but allows for high-fidelity study of disturbance growth. The inflow interpolation approach requires a converged baseflow solution for a separate upstream subdomain. Cell centered data is extracted at the outflow boundary of the upstream subdomain containing all primitive variables. This slice begins at the wall, spans the two symmetry planes, and extends to the freestream boundary surface. The computational plane is imposed as a Dirichlet boundary condition at the inflow ghost cells of the downstream subdomain. The location of the inflow interpolation plane is at $x/L = 0.23$ based on the characteristic length, $L = 0.369m$, defined from the stagnation point to the end of the geometry. The computational

plane location was chosen such that predicted N-factors from NPSE for the second mode and crossflow instabilities remain low upstream of $x/L = 0.30$. The boundary conditions are shown in Figure 1 and include a freestream uniform hypersonic inflow (hidden), isothermal wall with no-slip (grey), supersonic outflow (red), and symmetry planes (green) in the xy- and xz-planes to take advantage of the bilateral symmetry. The domain contains an extended expansion corner for improved representation of the flow conditions at the end of the experimental model. The isothermal wall is imposed since wind tunnel runs are relatively short duration and the magnitude of the surfacing heating is low. Therefore, the wall temperatures are expected to remain nearly constant. Even though there is a possibility of a finite amount of angle of attack and slideslip, the flow is assumed to be at zero degrees angle of attack and slideslip for simplicity. The grid is the same grid used in previous work [17] where the downstream subdomain contains approximately 390M total elements due to truncating the domain. The freestream flow conditions are listed in the Table 1 and were chosen from previous work such that breakdown was observed in the experiments conducted in the M6QT at Texas A & M University.

Table 1 Freestream Conditions

M_∞	U_∞ (m/s)	ρ_∞ (kg/m ³)	T_∞ (K)	T_{wall} (K)	Re/m (m ⁻¹)
6.0	871.09	0.0424	52.68	300	10.8×10^6

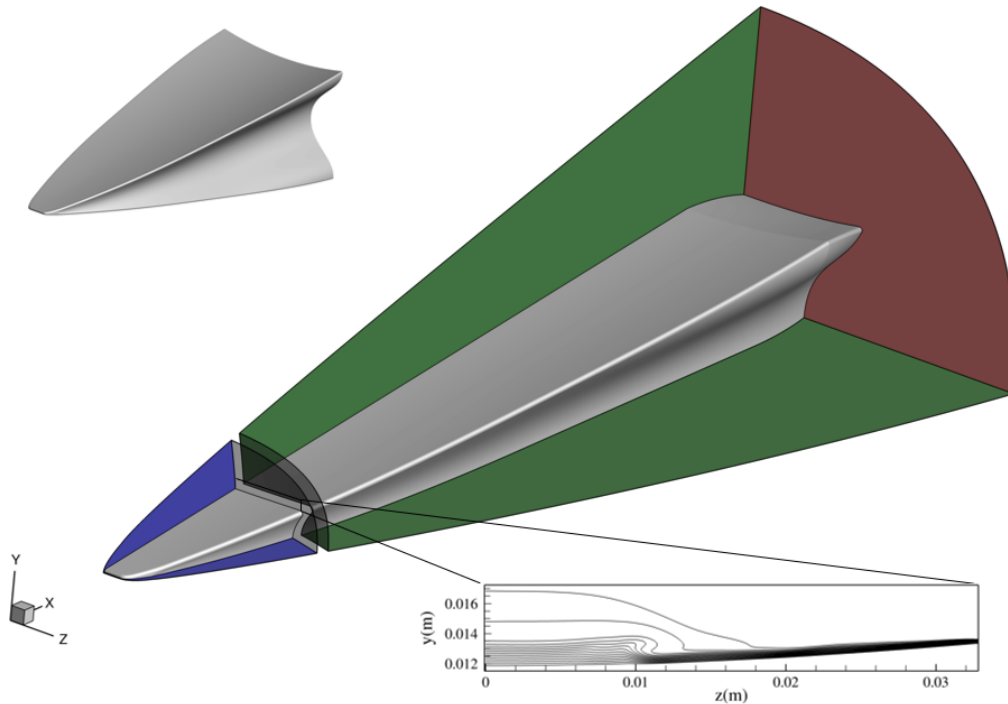


Fig. 1 Individual subdomains used for interpolated inflow with computational plane imposed as boundary condition onto the domain of interest.

C. Stochastic Forcing Approach

Before introducing controlled disturbances, a steady-state solution is fully converged before applying forcing to the baseflow state. The forcing approach is similar to the random forcing approach by Hader and Fasel [20] which is meant to simulate natural transition and was used in previous work [17]. This approach is meant to mimic freestream wind tunnel noise by introducing disturbances at the interpolated inflow boundary only. Therefore, the receptivity process is neglected to focus on investigating disturbance growth response due to boundary layer instabilities. The idea is to force with a wide range of frequencies to investigate breakdown so that there is not a bias towards a distinct instability mechanism. This is achieved by specifying a constant noise amplitude, A_{noise} , and using a pseudo-random number,

$r \in [0, 1]$, which is generated for each cell element when looping over the inflow cells of the computational plane and at every time step to apply a broadband range of frequencies. The random perturbations are directly applied to the pressure field at the forcing plane, the same computational plane as the imposed inflow interpolation boundary condition for ease of implementation. The density and temperature adjust to the pressure perturbations based on the linearized isentropic relations thereby assuming initial entropy fluctuations are negligible to satisfy the acoustic-mode.

In the past, environmental freestream characterization for wind tunnels have measured mass flux fluctuations $(\rho u)'$. There is uncertainty with the characterization of mass flux fluctuations for this forcing function that are representative of a quiet wind tunnel environment. Using the RMS voltage measurement from a hotfilm, Huntley [30] estimated a freestream mass flux fluctuation of 2% of the freestream mass flux fluctuation level for a conventional wind tunnel. It is well known for quiet wind tunnel environments that the freestream mass flux fluctuations are much lower. Therefore, a perturbation in velocity is applied to include a disturbance kinetic energy such that the maximum RMS mass flux fluctuations are reported to be less than 0.003% of the freestream mass flux. This makes it so that the fluctuations introduced are a discrete approximation of the spectrum with the pressure and velocity disturbances having the same noise amplitude. By setting the initial amplitude of the velocity disturbances equal to the noise amplitude, the mass flux fluctuations are the same order of magnitude as the estimate based on the density perturbations and convection velocity relation following Smits and Dussauge [31]:

$$\frac{(\rho u)'}{\bar{\rho} \bar{u}} = \frac{\rho'}{\bar{\rho}} \left(1 + \frac{1}{(\gamma - 1)M^2} \right). \quad (10)$$

The pressure disturbances are introduced in the following form:

$$p' = A_{noise}(2r - 1). \quad (11)$$

Fluctuations in the remaining flow variables are determined as:

$$\begin{pmatrix} \rho' \\ u'_i \\ T' \end{pmatrix} = \begin{pmatrix} \frac{1}{\bar{a}^2} \\ 1 \\ \frac{(\gamma-1)\bar{T}}{\bar{\rho}\bar{a}^2} \end{pmatrix} p'. \quad (12)$$

The forcing amplitude is chosen based off previous simulations by Johnston and Candler [17] using the proposed stochastic forcing approach. The forcing levels for the cases were defined using $P_{RMS} = RMS(\frac{p'}{\bar{p}})$ where p' is the fluctuating value of pressure and \bar{p} is the time-averaged value of pressure sampled. The fluctuating pressure levels of the input forcing were characterized by sampling various locations in the freestream lying on the forcing plane.

III. Steady flowfield

The baseflow was first computed using the freestream values of Table 1 to gain an understanding of the flow structures which exist in the flowfield. The three-dimensional flow features were first simulated and described in previous papers by Thome et al. [3, 32]. The nose of the geometry is a two-dimensional cylindrical leading edge that is revolved to a swept edge. The hypersonic flow around the surface curvature produces a strong bow shock curvature where it is postulated that a shock-shock interaction generates vorticity post-shock. Thome et al. [32] computed vorticity budgets quantifying the vorticity distribution in the near wall region. This produces varying pressure gradients close to the wall and developing vortex structures that are able to support various boundary layer instabilities. The most apparent structures are a pair of large-scale counter rotating vortex structures located on both sides of the centerline of the top surface. Between the centerline and swept edge, there is a high amount of localized vorticity where downstream developing stationary crossflow vortices become apparent. This has a direct affect on the surface heat flux where the varying thickness of the boundary layer produces heat flux streaks seen on the surface. A three-dimensional view in Figure 2 depicts this where planar slices show colored contours of streamwise velocity and the surface heat flux plotted using a grey-scale. Notice the heat flux gradients become more distinct with the development of stationary crossflow vortices. A qualitative comparison of the baseflow solution assumes laminar flow and therefore does not capture the same localized heating as seen in experiments. Experimental IR images reveal increased heating downstream originating near the stationary crossflow vortices. Even though some discrepancies are contributed by a finite amount of roughness and possible sideslip, the initial stages of nonlinear breakdown appear in this region motivating the current

work. Furthermore, Figure 2 shows a qualitative comparison of the surface heat flux with experiment. The experimental model shown is a surface finished 25% subscale 1.350m model truncated from the same 25% subscale 1.477m geometry used in simulation. The experimental model here was truncated to avoid a potential reflected shock interaction near the end of the geometry. Therefore, qualitative comparison shows similar heating effects except for a highly localized region near the stationary crossflow vortices. Previous simulations using the proposed computational methodology showed that higher forcing levels experience similar augmented surface heating effects observed in the time-averaged surface heat flux [17].

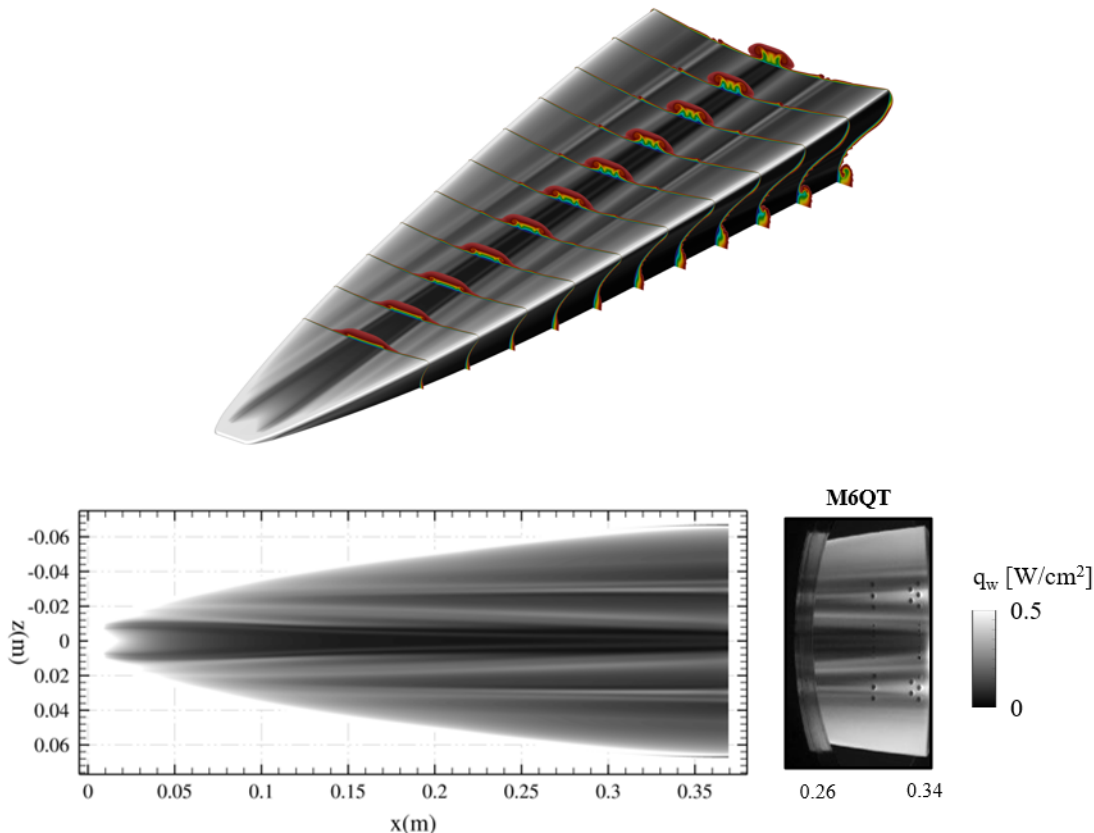


Fig. 2 Steady state flowfield and qualitative surface heating comparison to a surfaced finished subscale model at $Re/m = 10.8 \times 10^6$ freestream conditions.

IV. Forced Direct Numerical Simulation Results

Unsteady simulation results are obtained by introducing disturbances to the baseflow solution with the forcing approach described previously. Modal analysis in the later sections are performed on slice data collected from forced DNS data at lower forcing levels cases to avoid including fully turbulent regions in the analyzed datasets. A depiction of an instantaneous solution showing an instantaneous isosurface of the positive and negative streamwise velocity perturbations at a statistical steady state is shown in the Appendix.

A. Coherent Structures

To gain qualitative insight into the primary vortex structures that could support flowfield disturbances, we apply Q-criterion which defines a vortex as a connected fluid region with a positive second invariant in the divergence of velocity and requires the pressure to be lower than the ambient pressure in the vortex. This can be written as, $Q = \frac{1}{2}(\|\mathbf{\Omega}\|^2 - \|\mathbf{S}\|^2) > 0$, where $\mathbf{\Omega}$ and \mathbf{S} are the antisymmetric and symmetric components of the velocity gradient tensor [33, 34]. Figure 3 shows an isosurface for a single value of $Q = 10,000$ and colored by instantaneous local temperature revealing coherent structures. This reveals a range of length scales and the large-scale vortex is apparent

near the centerline. Moving outboard there are wave-like structures propagating in the flow direction, and appear trapped between the wall and boundary layer edge located on both sides of the developing stationary crossflow vortex structures. The structures originate upstream in the vicinity of where second-mode was identified on BoLT in the past. Furthermore, the development of small-scale streamwise vortices produce a steady isosurface located near the crossflow vortical structure. Towards the end of the geometry there is a formation of a supporting instability leading to breakdown for the lower forcing level case. This is depicted by turbulent onset with the development of hairpin-shaped structures. This becomes more apparent with the increase in forcing level as shown in Figure 4. Breakdown to the small-scale coherent structures represents fully turbulent regions and appear when applying a large initial disturbance amplitude spectrum. Additionally with the increase in forcing level, secondary flow effects in the region of the oblique oriented vortex structures are observed and precedes the fully turbulent region seen by the $P_{RMS} = 0.5\%$ case. Therefore, qualitative comparison shows the turbulent front begins to march forward with an increasing forcing amplitude spectrum using the same computational methodology. Even though receptivity is neglected, this reveals the importance of using a low dissipation numerical method with an external forcing function to allow disturbances to grow in a physical manner representative of natural transition. Additionally, the importance of initial disturbance amplitude can directly impact instability excitation and is governed by the numerical scheme and grid resolution.

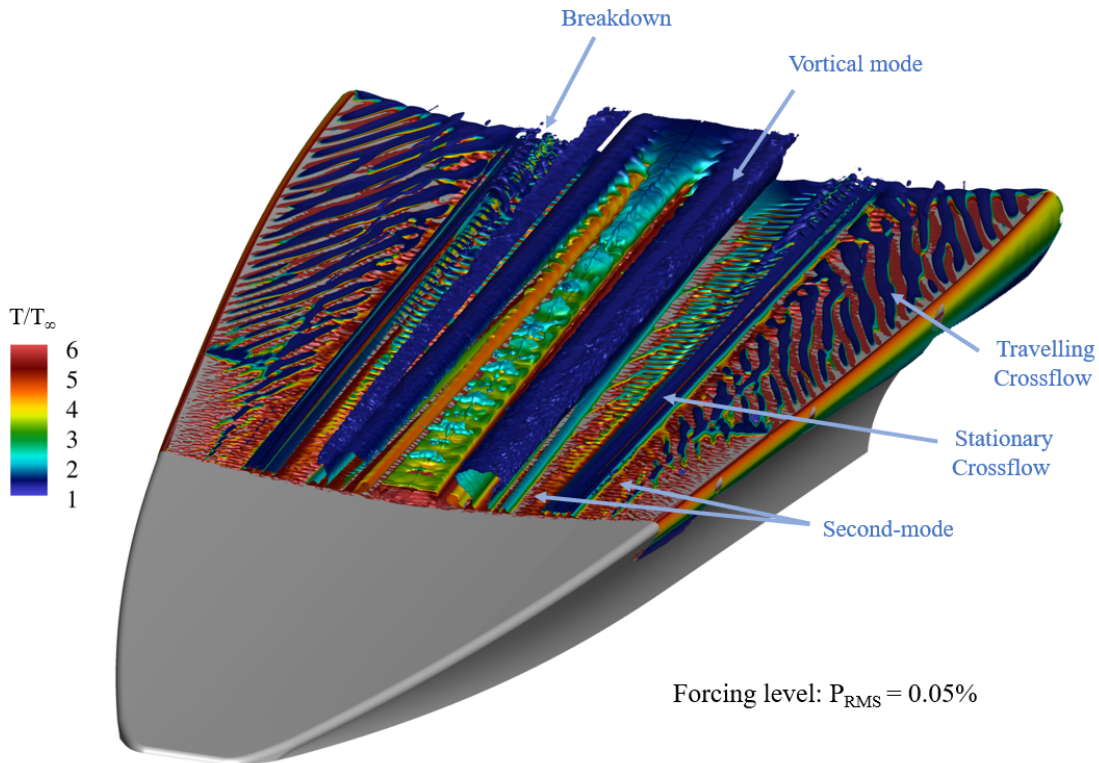


Fig. 3 Qualitative identification of vortex structures based on Q-criterion with a single isosurface ($Q=10,000$) colored by local temperature.

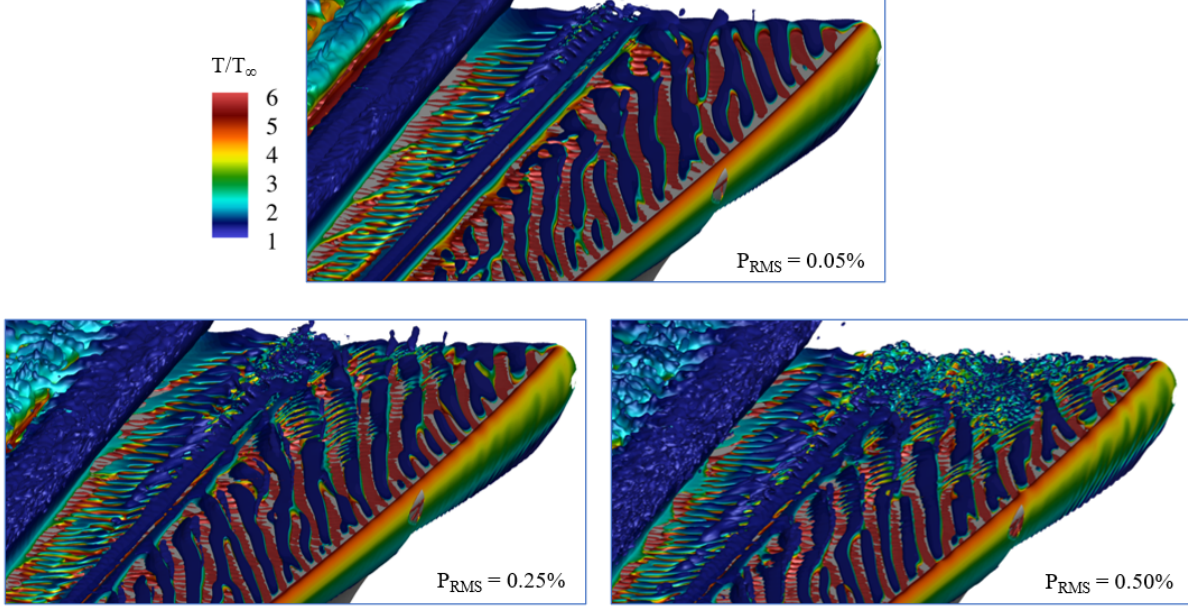


Fig. 4 Comparison of Q-criterion isosurface plots for $Q=10,000$ and colored by temperature for varying forcing levels.

B. Compressible Energy Distribution

Decomposing this flowfield in a manner consistent with the computational methodology is unclear due to the complexity of the flowfield and geometry. Therefore to help circumvent disturbance amplification, the time-averaged disturbance energy amplitudes is computed. Because the data is collected from DNS, the simulation dataset in theory includes linear and nonlinear flow processes along with mode interactions since it is assumed that the solver is able to simulate the effects based on previous work of our group. To quantify nonlinear disturbance growth, the compressible energy distribution was computed with a norm of the perturbation chosen to account for disturbance energy in a compressible flow. For the present work, the transfer of disturbance energy from a steady main stream was selected based on the positive definite energy norm first introduced by Chu [35–37]. This is an intrinsic energy norm for the study of boundary layer analysis since it is consistent with characterizing disturbance fluctuation by considering kinetic, acoustic, and internal energy contributions.

The Chu energy norm is defined as,

$$E_{CE} = \int_{\Omega} \left(\frac{1}{2} \bar{\rho} u'_i u'_i + \frac{\bar{p}}{2} \left(\frac{\rho'}{\bar{\rho}} \right)^2 + \frac{\bar{E}_{int}}{2} \left(\frac{T'}{\bar{T}} \right)^2 \right) d\Omega. \quad (13)$$

The overbar signifies the quantities associated with the baseflow, and the prime values are the disturbance quantities calculated by subtracting the baseflow value from the instantaneous value. The term inside the integral of Equation (13) has units of energy per unit volume and the integral is over a single grid element. Because we have cell centered data using a finite volume method, we compute the energy within a cell by simply multiplying by the cell volume in the discrete form since the cell centered values are taken to be the average value across a cell. This is a second-order accurate calculation for the energy over a cell volume using the numerical methodology. The instantaneous total energy across a cell is computed at each instance in time and then the value is averaged in time.

Figure 5 shows the compressible disturbance energy distribution for slices taken at separate streamwise locations. Notice that the maximum value grows over three orders of magnitude from $x/L = 0.740$ to $x/L = 0.979$ near the stationary vortex structure revealing the local nonlinear disturbance growth. Instantaneous surface pressure perturbations show an imprint of boundary layer instabilities relative to the increase in energy off the wall. The same datasets used for modal analysis are used for this calculation and data collection is summarized in Table 3 of the Appendix.

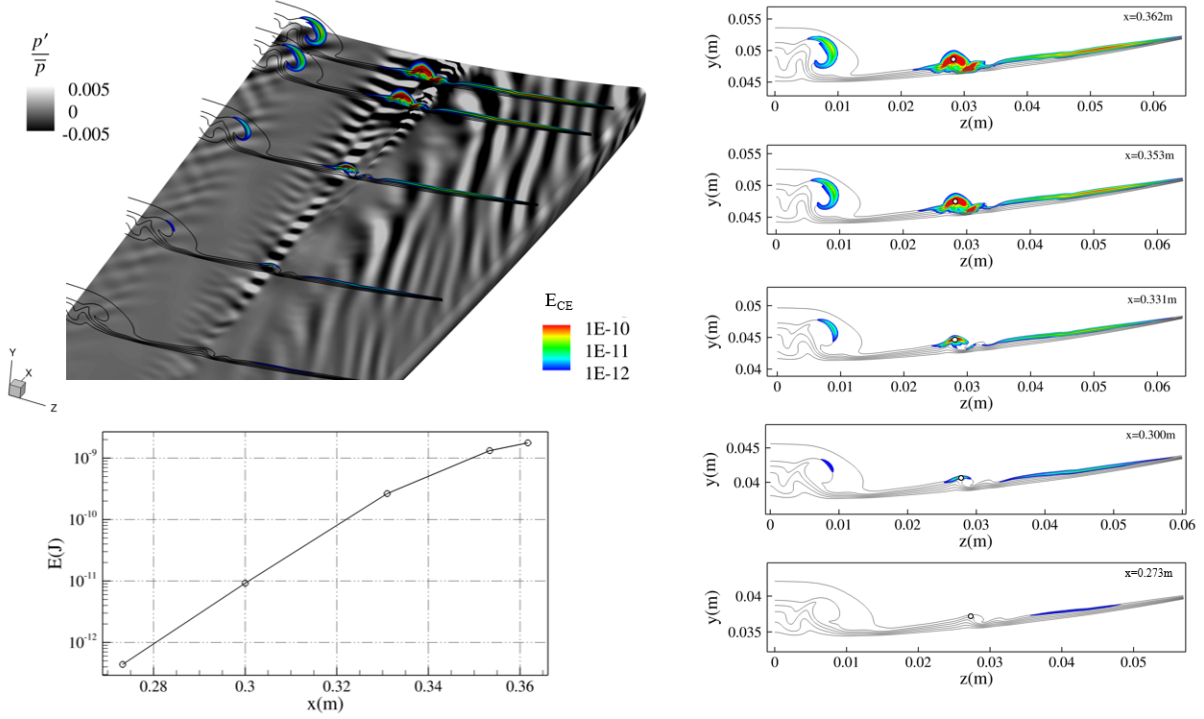


Fig. 5 Disturbance compressible energy distribution for $P_{RMS} = 0.05\%$ forcing level. Top left shows slices taken at $x/L = 0.740, 0.812, 0.896, 0.957, \text{ and } 0.979$ with contour lines corresponding to streamwise velocity and colored contours of the energy plotted on a log-scale. Bottom left are probed local maximum values near the primary stationary vortex structure with respect to the slices as shown on the right.

V. Dynamic Mode Decomposition Methodology

The general idea of dynamic mode decomposition (DMD) is to decompose the flowfield in terms of its dynamics by deconstructing a sequence of snapshot data into a set of spatial modes, each with an associated frequency and growth/decay rate. When these modes are combined, they form a low-order representation for the dynamics underlying the original dataset. The method assumes there is an underlying linear dynamical system that governs the evolution between snapshots. The data consists of a sequence of $M+1$ snapshots spaced a fixed Δt apart,

$$\{\psi_0, \psi_1, \dots, \psi_M\}$$

where $\psi_i \in \mathbb{R}^N$ is a column vector denoting the i -th snapshot. The N components in each snapshot correspond to the total number of states (i.e., cell centered values) that define the flow state at a given instant in time. Next, two data matrices are formed from the original snapshot sequence:

$$X := [\psi_0, \psi_1, \dots, \psi_{M-1}] \in \mathbb{R}^{N \times M}$$

$$Y := [\psi_1, \psi_2, \dots, \psi_M] \in \mathbb{R}^{N \times M}.$$

Following the definition in Tu et al. [38], the DMD modes and eigenvalues are determined from a best-fit/minimum norm linear mapping, $A \in \mathbb{R}^{N \times N}$, satisfying the snapshot data relation:

$$A_{DMD} := YX^+. \quad (14)$$

Here, X^+ denotes the Moore-Penrose pseudoinverse of X . We note that the eigendecomposition of an $N \times N$ matrix scales with $O(N^3)$, and so this can be an expensive calculation when N is large.

In practice, it is more computationally expedient to work with a low-dimensional proxy system through a projection onto an r -dimensional subspace \mathbb{R}^r , where $r < N$. The standard approach for performing this projection involves a

singular value decomposition (SVD), which can introduce a heavy memory/storage requirement for large snapshot matrices. A low-storage “streaming” formulation of the DMD algorithm was proposed in [39] to overcome this issue for large datasets. Although the streaming DMD algorithm enables analysis of large datasets, the method can be fragile to noise and round-off error. A noise-robust variant of the streaming DMD algorithm was proposed in [40], which extended the noise-robust total DMD method of Hemati et al. [41] into a low-storage single-pass method. In the present work, we will make exclusive use of the streaming total DMD (STDMD) algorithm because it is low-storage and provides a more reliable analysis of our stochastically forced DNS data than the original streaming DMD algorithm. A freely available software implementation of the STDMD algorithm was used in this work [42].

A. Compressible Energy Norm Weighting

Before performing STDMD, we make a change of coordinates of the snapshot data to be consistent with the Chu energy norm with respect to the baseflow state. Following Dwivedi [43], we can rewrite the energy norm from (13) in terms of a vector of primitive fluctuation variables, $q = [\rho' \quad u'_i \quad T']^T$, as

$$E_{CE} = \int_{\Omega} q^T \mathbf{M} q \, d\Omega, \quad (15)$$

where the weight matrix, \mathbf{M} , is defined as,

$$\mathbf{M} = \begin{bmatrix} \frac{\bar{p}}{2\rho^2} dV & 0 & 0 & 0 & 0 \\ 0 & \frac{\bar{p}}{2} dV & 0 & 0 & 0 \\ 0 & 0 & \frac{\bar{p}}{2} dV & 0 & 0 \\ 0 & 0 & 0 & \frac{\bar{p}}{2} dV & 0 \\ 0 & 0 & 0 & 0 & \frac{\bar{E}_{int}}{2T^2} dV \end{bmatrix}. \quad (16)$$

Because the cell centered data are scalar values, the transformation is simply a weighting of the primitive flow variables with the transformation being related to the matrix square root of the weight matrix inside the norm itself. A consideration of the cell volumes is very important here as each cell carries its own weight of information that is contributing to the total energy of the system. In order to make the modal analysis consistent with the Chu energy norm, we apply the linear transformation,

$$\tilde{q} = \mathbf{M}^{\frac{1}{2}} q, \quad (17)$$

where the vector of disturbance fluctuations now includes the energy norm weighting,

$$\tilde{q} = \begin{bmatrix} \rho' \sqrt{\frac{\bar{p}}{2\rho^2} dV} \\ u' \sqrt{\frac{\bar{p}}{2} dV} \\ v' \sqrt{\frac{\bar{p}}{2} dV} \\ w' \sqrt{\frac{\bar{p}}{2} dV} \\ T' \sqrt{\frac{\bar{E}_{int}}{2T^2} dV} \end{bmatrix}. \quad (18)$$

Then, the Euclidean norm of \tilde{q} gives the compressible energy of a cell, i.e.,

$$E_{CE} = \tilde{q}^T \tilde{q}. \quad (19)$$

This allows us to use STDMD to identify the dynamics of boundary layer modes underlying the response of the Chu disturbance energy.

The dominant mode is the same for all field variables since the simulation is statistically converged and STDMD is performed on the full flow state, which contains all of the field variables. Plotting mode shapes for different flow variables reveals the growth or decay of local perturbation quantities as well as the strength of a flow variable for a particular mode. Spatial structures are consistent with simply performing DMD on the raw fluctuation data. However, temporal quantities (i.e., frequencies and growth rates) computed from the eigenvalues of the raw data without the energy

norm weighting are not consistent with growth of disturbances induced by boundary layer transition mechanisms. The eigenvalues of the modes computed from raw fluctuation data are often damped modes resulting in decay rates. Whereas, the linear transformation yields physically meaningful growth rates, since the resulting coordinate system for the analysis is consistent with the Chu energy norm. Therefore, STDMD is performed on \tilde{q} to provide an improved approximation of frequencies, growth rates, and mode selection. This makes it so that dominant modes are identified considering five flow variables and their contribution to the kinetic, acoustic, and internal energies relative to the baseflow state.

B. STDMD Rank Threshold

To determine the proper rank threshold, the integrated disturbance energy norm, E , is computed as a function of time through a summation of all elements which make up a slice. The power spectral density (PSD) of the signal is computed where it was found that peaks values that do not drop below two orders of magnitude, relative to the highest peak value, identified modes having large relative DMD amplitudes with frequencies consistent with surface pressure PSD peaks. Therefore, the PSD of the energy norm is primarily used to dictate the number of modes to retain as determined by the rank threshold. The discrete Fourier transform is computed from the energy norm signal where the peaks in the frequency spectrum corresponds to nonlinear flow processes. This provides frequency ranges of the flow processes spanning the region in time where the highest peaks have frequencies consistent with the relevant modes identified by STDMD. However, the highest peak value, $|\hat{E}|$, does not necessarily correspond to a more physically significant STDMD mode as seen in Figure 6. The frequency spectrum only provides an estimate for expected mode frequencies by making a direct comparison to the extracted modes at various truncation levels. The proper truncation level was selected such that the same dominant modes are identified between various truncation levels where the frequencies resemble the frequency spectrum peaks of the energy norm. By computing the PSD and frequency spectrum of the energy norm, we are able to identify an estimate for the number of modes to retain while providing an estimate of expected mode frequencies. The relative DMD amplitudes are used to order the modes and the ordering is consistent with surface pressure PSD measurements from experiment and simulation.

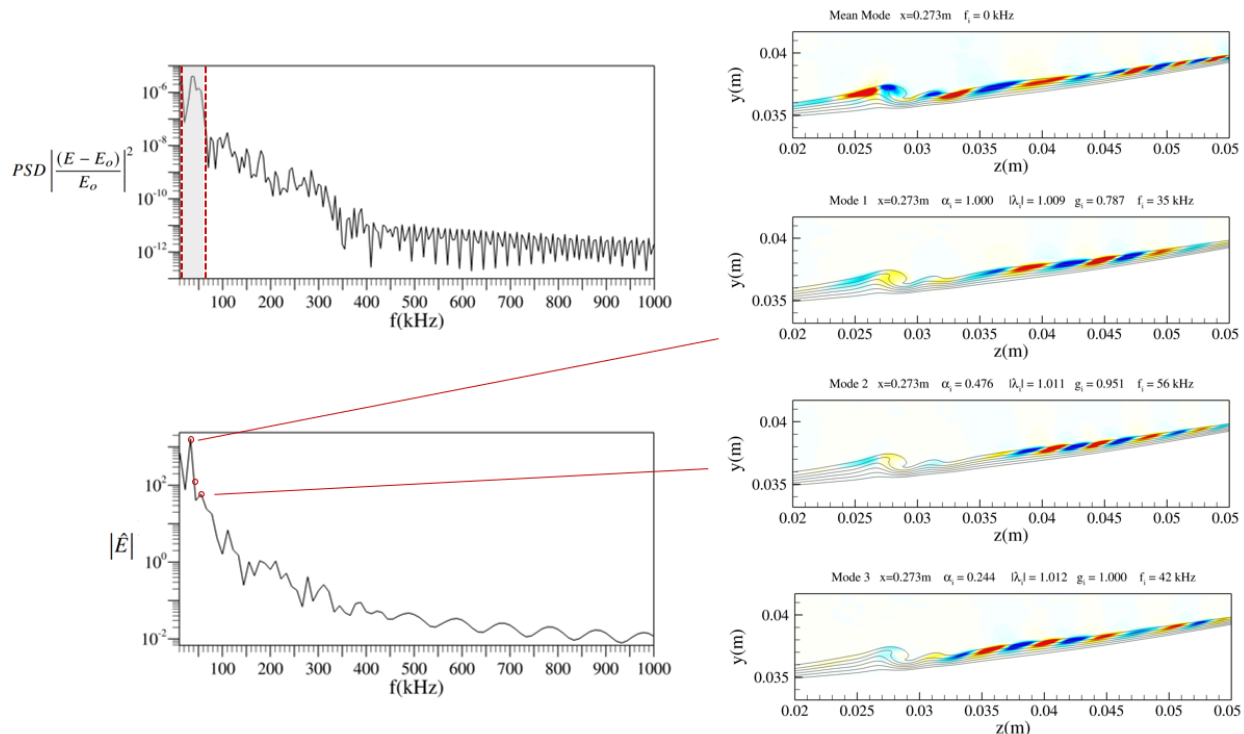


Fig. 6 Mode identification used for selecting truncation level.

"o" denotes time averaging of, E , the energy norm integrated over all elements that construct a slice.

One should be aware that an under-truncation (i.e., high rank threshold) of the STDMD spectrum can lead to

spurious modes which arise as numerical artifacts. This is thought to be caused by over fitting the linear operator due to propagating broadband wavenumber content associated with the stochastic forcing function. To the contrary, an over-truncation (i.e., low rank threshold) of the spectrum will lead to modes not being retained that could have a significant contribution to the increase in local disturbance energy. It is important to retain all physically relevant modes since they have greater contribution to the increase in compressible energy and ultimately the flow dynamics.

VI. Spatio-temporal Analysis

The data sets in this section span regions including nonlinear flow effects to demonstrate how well the approach identifies modes but does not include fully turbulent onset as identified by the small-scale coherent structures of Figure 4. Previously, Shrestha and Candler [44] performed a two-dimensional computation on trip induced transition of boundary layer roughness elements using SPDMD and the Chu energy norm for mode selection. DMD modes qualitatively represented transition mechanisms, but the linear mapping between consecutive snapshots was not accurate since the dataset included regions where the flow was fully turbulent or experienced nonlinearity. This was observed in the present work when including fully turbulent regions, but consistent modes were still extracted for regions when including nonlinear flow effects. The work by Knutson et al. performed modal analysis on truncated slice data showing the dominant mode at a particular location. This is useful for isolating modes contributing to linear growth of boundary layer instabilities, but does not allow a direct comparison of DMD modes in the spanwise direction and at the same streamwise location. Therefore, we show that STDMD with the energy norm weighting approach is able to identify modes contributing to transition in the initial stages of breakdown without making the prior assumption as to where flow transition originates. This allows us to make a direct comparison of which mode has a more significant contribution to the flow dynamics in the presence of breakdown by ordering the modes in terms of relative DMD amplitudes. The following results show modes contributing to transition and the dominant modes identified to primarily initiate breakdown before turbulent onset at subscale conditions with a comparison to experiment.

A. Leading Boundary Layer Modes

Using the energy norm weighting and mode identification, dominant boundary layer modes are extracted at five streamwise locations for the $P_{RMS} = 0.05\%$. For brevity, the first 3 dominant mode shapes of streamwise velocity are shown for the remaining four slice locations downstream. Since we have competing instabilities dependent on local boundary layer properties, there are modes which have varying amounts of growth rates meaning that particular modes may be contributing more to the local energy than other modes at different streamwise locations. Therefore, the modes exist but are not deemed to have a physically significant contribution to the flow dynamics as identified by STDMD and at a particular streamwise location. All the modes in the paper are identified away from the large-scale centerline vortex. This is due to the fact that the disturbance values are largest in the regions identified in Figure 5 even though the data is included in the analysis. Figure 7 shows that the leading dynamics modes at $x/L=0.812$ are primarily located outboard. The spatial structures are located on the left side of each figure and correspond to the real component of the eigenvectors computed from the linear operator. The magnitude of the real and imaginary components of the eigenvectors are plotted on the right side of each figure. The discrete values above each plot are computed from the eigenvalues where $|\lambda_i|$ is the magnitude of the corresponding eigenvalue:

Frequencies,

$$f_i = \Im \lambda_i / (2\pi \delta t) \quad (20)$$

Growth Rates,

$$g_i = \log |\lambda_i| / \delta t \quad (21)$$

The mode shapes at $x/L = 0.812$ resemble the mode shapes extracted by Knutson et al. where the dominant mode here has a frequency of $35kHz$. Therefore, this mode is consistent with traveling crossflow in terms of mode shape and frequencies. In fact, all leading modes appear to be associated with traveling crossflow at this streamwise location. Interestingly, the third dominant mode has a higher frequency of $69kHz$ and is primarily located near the stationary crossflow vortices according to the magnitude of the eigenvectors seen on the right. The frequencies of these modes are consistent with the local frequencies computed for traveling crossflow using NPSE by Mullen and Reed [18]. The magnitude of the eigenvalues, $|\lambda_i|$, are all positive suggesting that all the modes at $x/L = 0.812$ are unstable and growing in time.

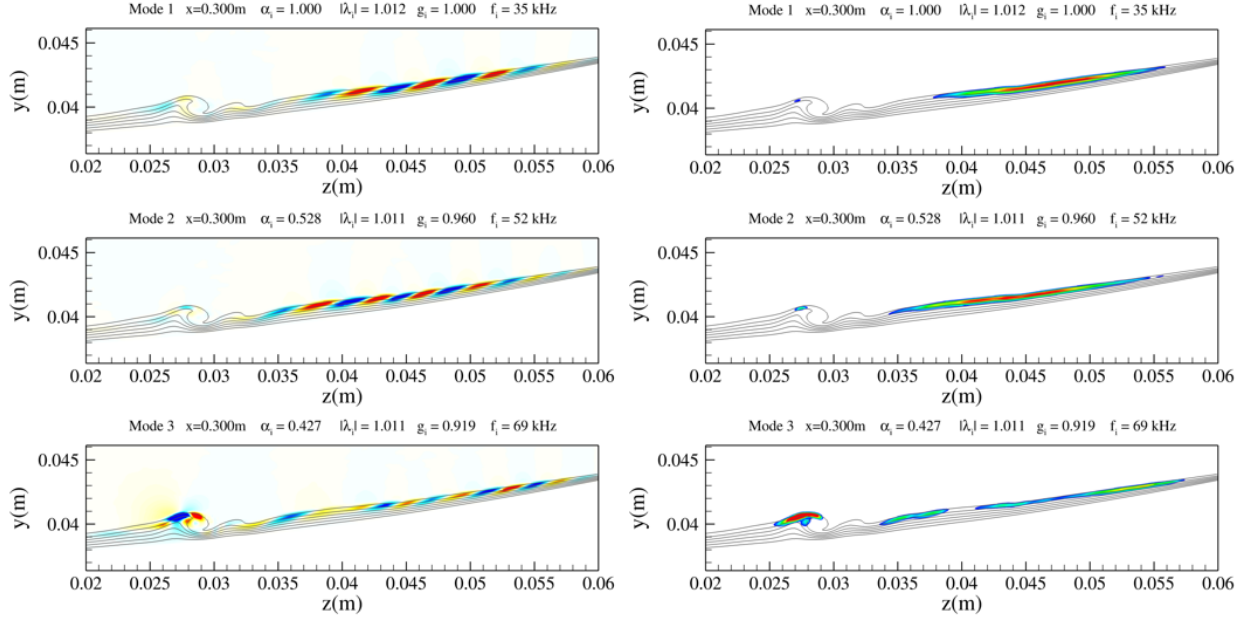


Fig. 7 Leading STDMD modes of streamwise velocity extracted at $x/L = 0.812$. Real component of the eigenvectors with positive values denoted as red and negative values as blue (left). Magnitude of the eigenvectors (right) with the larger value represented with red (right).

The traveling crossflow modes having frequencies in the range of 35kHz and 52kHz are also identified as leading modes downstream at $x/L = 0.896$. The mode shapes of the magnitudes reveal that the modes are primarily active closer to the swept edge. Notice that the magnitudes show these modes are not only active outboard but near the stationary crossflow vortex as well. This is due to the fact that a single DMD mode can represent multiple transition processes happening at the same discrete frequency. Therefore, this reveals that crossflow modes are beginning to have a more significant contribution on the inboard side of the stationary crossflow vortex. However, the mode with the largest contribution on the increase in disturbance fluctuation has a frequency of 176kHz and is highly localized on the top portion of the stationary crossflow vortex where there is a high amount of shear. At this location, flow is experiencing nonlinear energy growth as seen previously from Figure 5.

Similar to upstream, a high frequency mode is identified to be the dominant mode at $x/L = 0.957$ and $x/L = 0.979$ with a frequency 185kHz and 190kHz , respectively. The spatial structures are slightly different than the previous dominant mode but are all highly localized near the stationary crossflow vortex. This suggests the high frequency mode is the dominant mode contributing to transition. A range of discrete frequencies of this mode are most likely contributed by the fact that the analysis is performed on each streamwise location independently as well as the local flow properties vary spatially. Depending on the forcing level, spatial location, and rank threshold, this mode was found to vary in frequency between 175 to 210kHz and has been identified as the dominant mode beginning at approximately 90% of the geometry length. It is worth noting that modes primarily associated with crossflow are still identified as leading modes and have frequencies ranging from 30 to 60kHz . The modes are primarily located outboard near the swept edge. However, signatures are identified near the dominant mode due to the flow experiencing turbulent onset.

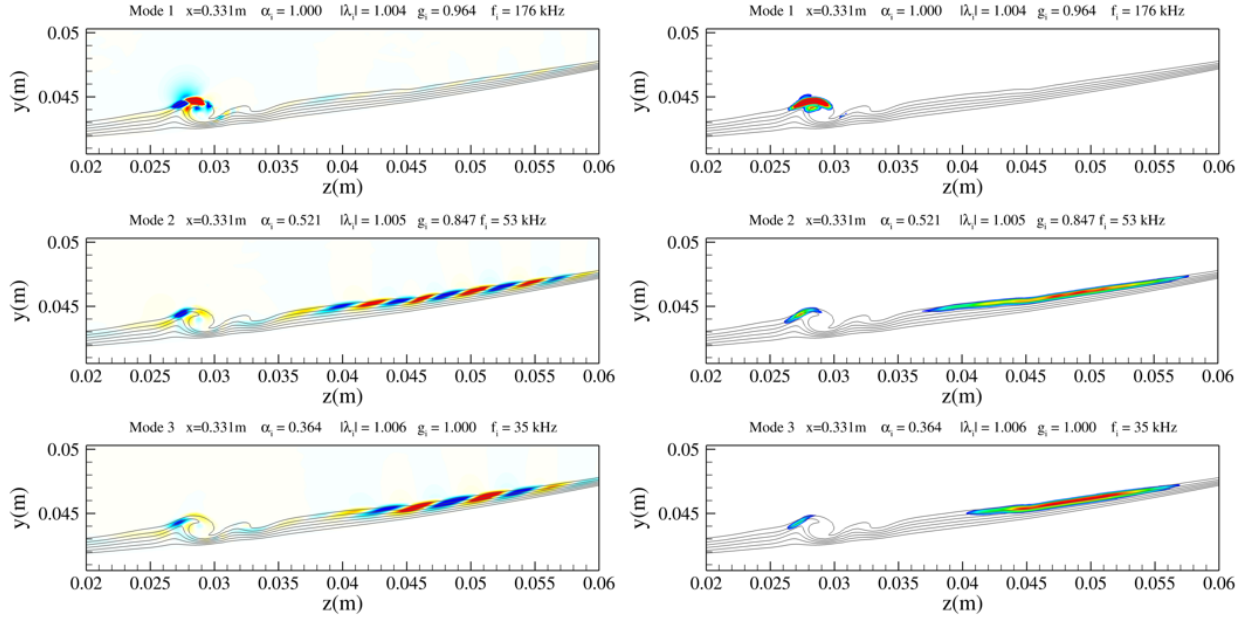


Fig. 8 Leading STDMD modes of streamwise velocity extracted at $x/L = 0.896$

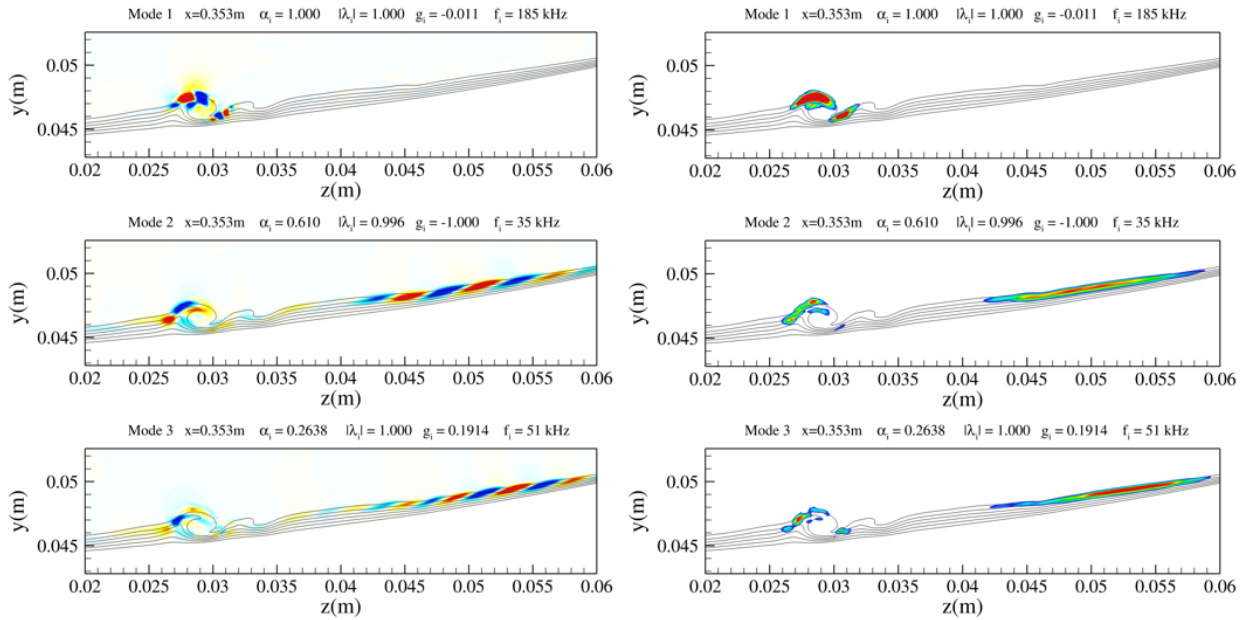


Fig. 9 Leading STDMD modes of streamwise velocity extracted at $x/L = 0.957$

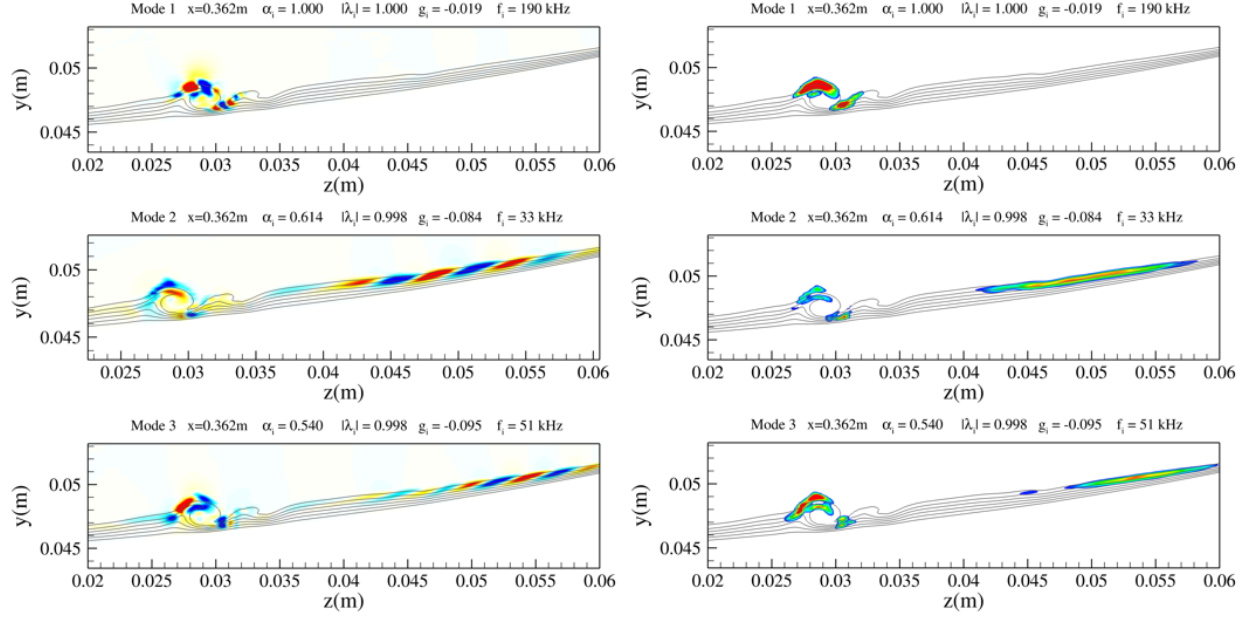


Fig. 10 Leading STDMD modes of streamwise velocity extracted at $x/L = 0.979$

In order to characterize local wave properties of crossflow, the same methodology following Knutson et al. was performed. The spatial structures active outboard of the stationary crossflow vortices are used to obtain a spanwise wavelength, λ_ζ . The wave angle, ϕ , is defined as the angle between the boundary-layer edge velocity vector and the phase velocity vector. The wave angle is approximately 73° near the swept edge but varies spatially further inboard where the leading modes are identified. The wavelength, λ , is the distance between wave fronts in the direction of propagation:

$$\lambda = \lambda_\zeta \sin\phi \quad (22)$$

The local phase speed, c_{ph} , is computed from the STDMD mode frequency and wavelength as $c_{ph} = f\lambda$. The phase speed is non-dimensionalized by the boundary layer edge velocity, u_e . The scaling of the wave properties are consistent with traveling crossflow and are a function of wave angle, wavelength, boundary layer thickness δ , and boundary layer edge velocity. All of which are flow quantities that vary spatially due to varying velocity and pressure gradients. Therefore, the values of $\phi, \lambda_\zeta, \delta$, and u_e were taken at the maximum magnitude of the streamwise velocity modes.

Table 2 Local Wave Properties of Crossflow Modes

x/L	Mode	$f(kHz)$	$\phi(deg)$	$\lambda(mm)$	$\delta(mm)$	$u_e(m/s)$	λ/δ	$f\delta/u_e$	c_{ph}/u_e
0.740	1	35	66	1.1	0.84	753	1.3	0.039	0.05
	2	56	70	3.3	0.95	753	3.5	0.070	0.25
	3	42	70	3.3	1.14	761	2.9	0.063	0.18
0.812	1	35	73	5.0	0.90	758	5.5	0.042	0.23
	2	52	69	1.4	0.99	750	1.4	0.069	0.10
	3	69	72	1.6	0.73	753	2.2	0.067	0.15
0.896	2	53	67	3.9	1.02	755	3.8	0.072	0.28
	3	35	67	4.8	0.97	757	4.9	0.045	0.22
0.957	2	35	70	3.9	0.99	765	4.0	0.045	0.18
	3	51	67	4.4	1.08	745	4.1	0.074	0.30
0.979	2	35	72	1.8	1.15	753	1.6	0.050	0.08
	3	51	74	4.6	0.98	753	4.7	0.066	0.31

B. Modal Interaction of Instabilities

Perturbations in the region revealing nonlinear energy growth are comprised of multiple modes as seen in the previous section. Looking more closely at the high frequency mode contributing the most to the flow dynamics, we can plot the modes of the individual flow variables to gain a better understanding of local flow dynamics. Figure 11 shows the streamwise velocity and density are correlated and the temperature is anti-correlated with positive and negative eigenvector values denoted as red and blue, respectively. On the inboard side of the primary stationary crossflow vortex, the u - and w -velocity perturbations are positive and v -velocity perturbations are negative. The opposite effects are observed on the outboard side. This suggests the stationary crossflow vortex is supporting large amplitude disturbances taking the form of strong vortical disturbances localized on top of the structure. The perturbations of w -velocity have a slightly larger amplitude than the v -velocity component. The w -velocity disturbance mode shapes of traveling crossflow have shown strong signatures with the v -velocity disturbance mode shapes located primarily outside of the boundary edge. Therefore, the presence of the strong v -velocity disturbance signature suggests that this mode is not characterized solely by traveling crossflow. Second mode waves appear to be present in this region as identified by Figure 3 and evidence of second mode frequencies are computed from surface PSD peaks in both simulation and experiments. Therefore, the high frequency mode appears to be associated with a modal interaction where disturbances are supported by the stationary crossflow structures.

In experiments, the pressure transducer denoted as P1 measured a PSD peak between 175 to 210kHz and varies depending on Reynolds number located at $x/L \approx 0.957$. Previous work showed the initial forcing amplitude can vary the PSD peak on the surface as well. The dominant mode identified by STDMD using a forcing level of $P_{RMS} = 0.05\%$ has a strong signature located above the location of the sensor with a $f = 185\text{kHz}$. Even though the modes of the previous section correspond to streamwise velocity, the mode shapes of all the primitive flow variables show strong signatures highly localized in the same region. Therefore, the mode shapes are sufficient for comparison to wall pressure power spectral density peaks. The experimental PSD peak range is consistent with the frequency of the mode identified to have the strongest contribution on the flow dynamics. Therefore, suggesting it is the main source of nonlinear disturbance growth in the region experiencing breakdown in experiments.

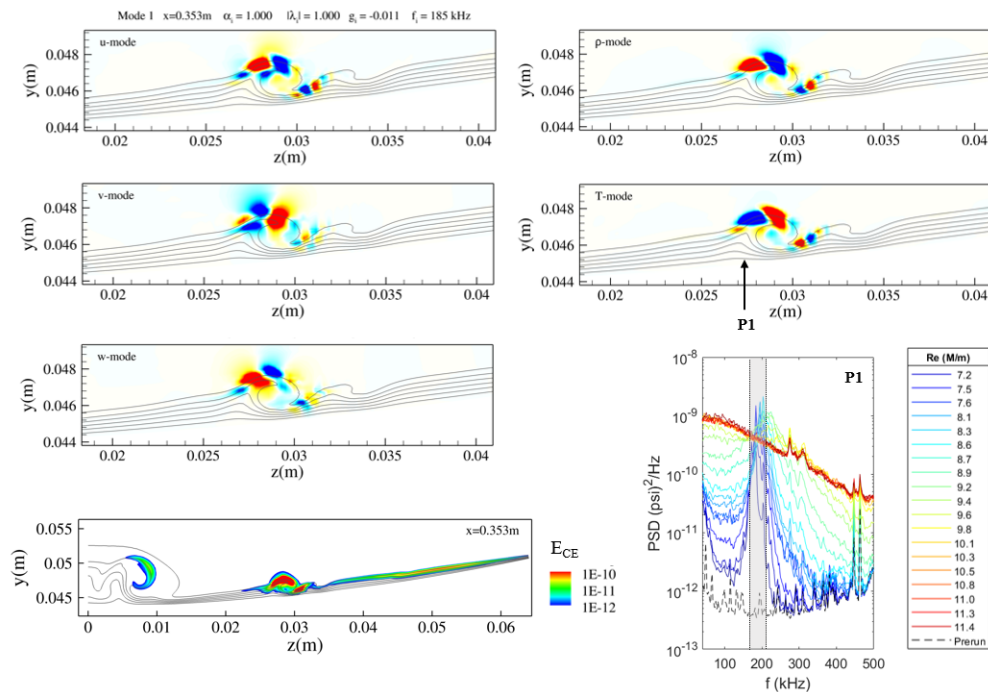


Fig. 11 Mode shapes of three components of velocity, density, and temperature. Lower left is the time averaged compressible energy distribution plotted on a log-scale. The lower right shows a PSD peak measured by a surface pressure sensor where colored lines correspond to increasing Reynolds Number.

C. Secondary Flow Behavior of Crossflow

Previous work showed an increased in time-averaged surface heat flux with increased heating occurring closer to the swept edge producing a diamond shaped heating pattern [17]. Figure 4 revealed that instabilities develop on top of the primary traveling crossflow structures which precedes the small-scale coherent structures. The flow effect is apparent in both the $P_{RMS} = 0.25\%$ and $P_{RMS} = 0.5\%$ forcing level cases, with the higher forcing level cases initiating turbulent onset set further upstream. To gain more insight of this flow effect, truncated slice data was collected away from the fully turbulent region for the $P_{RMS} = 0.25\%$ case at $x/L = 0.979$ between $z = 0.036m$ and $z = 0.063m$. The modes extracted varied from 12 to 61kHz depending on the truncation level. The first and the third modes are shown in Figure 12 with the mode shapes of u -, v -, and w -velocity components. The magnitude of Mode 2 identified by STDMD is much lower than Mode 1 and Mode 3 and located away from the location outboard of $z = 0.045m$. Therefore, Mode 2 is not shown. Mode 1 and Mode 3 show strong signatures located between $z = 0.036m$ and $z = 0.045m$ and near the region experiencing a large increase in compressible energy. The mode shapes for Mode 1 are consistent with the traveling crossflow modes shown previously but with a lower frequency of $f = 27kHz$. As for Mode 3, the mode shape is significantly different with the spatial structure showing evidence of smaller wavelength structures and at a frequency, $f = 60kHz$, approximately twice the frequency of Mode 1. The mode shapes for v - and w -velocity components show strong signatures and are localized above and below the spatial structures of Mode 1. This suggests secondary flow effects are developing on top of the primary mode representing crossflow and precedes the turbulent onset closer to the swept edge.

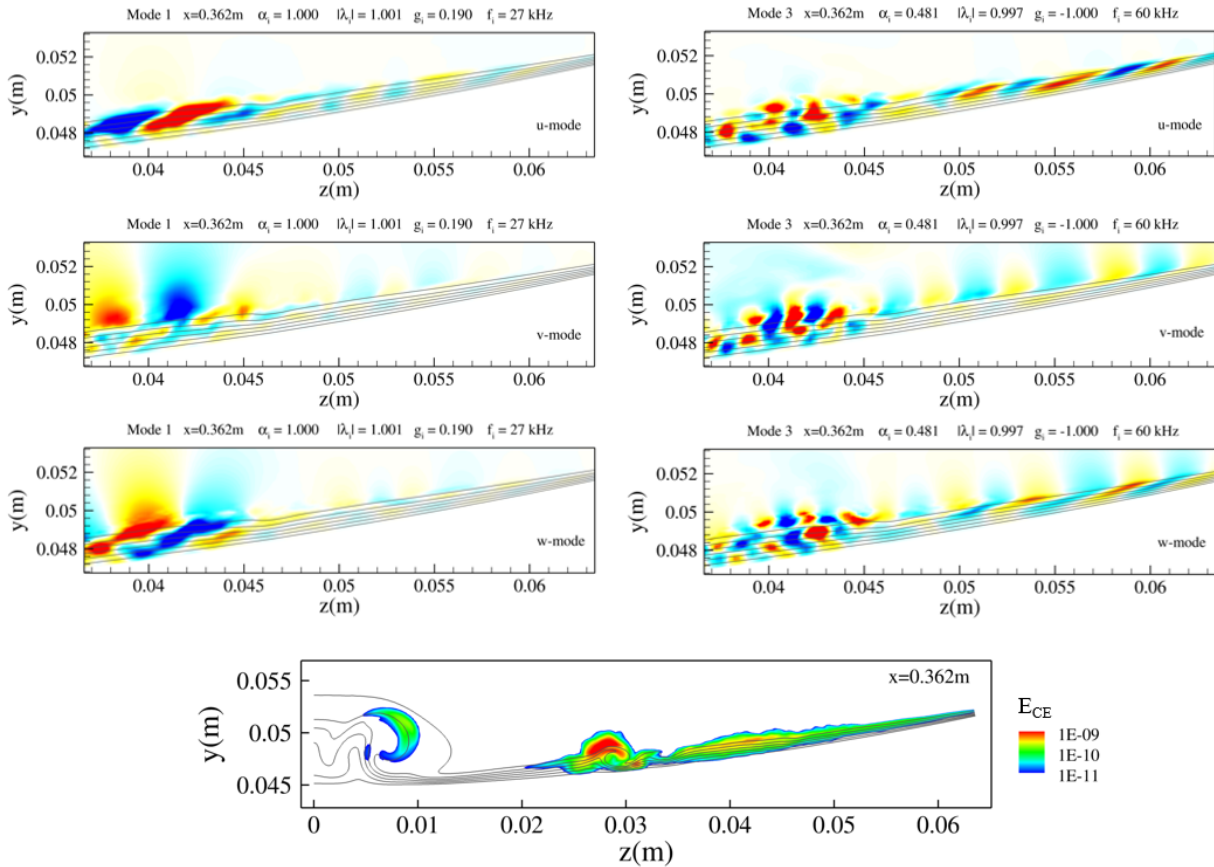


Fig. 12 Mode shapes of three components of velocity Mode 1 (left) and Mode 3 (right) located outboard of stationary crossflow vortices at $x/L=0.979$ with $P_{RMS} = 0.25\%$ forcing level. Time averaged compressible energy is plotted on a log-scale (bottom).

VII. Conclusion

We have shown that by following the proper numerical methodology, the stochastic forcing approach can be used to simulate natural transition of the BoLT-2 flowfield using a zonal DNS approach. Furthermore, high-fidelity solutions of the Navier-Stokes equations are obtained using a carefully generated grid with improved manual shock alignment and accurate resolution that are sufficient to capture high frequency flow processes. This is achieved using a combination of low-dissipation fluxes and a shock capture method that tailors numerical dissipation at the bow shock and regions experiencing numerical instability due to high amplitude disturbances. Therefore, the proposed computational methodology is capable of simulating natural transition and predicting unsteady disturbance response within three-dimensional hypersonic boundary layers.

Introducing controlled disturbances representative of quiet wind tunnel noise has enabled the study of nonlinear disturbance growth using an approach consistent with experiments. Streaming total dynamic mode decomposition with a compressible energy norm weighting has been used to extract DMD modes associated with boundary layer transition processes from the forced DNS data obtained using a sufficient sampling rate. The leading modes identified using the modal analysis methodology has allowed us to identify various crossflow modes with corresponding frequencies, wavelengths, and wave angles. The dominant mode appearing later in the transition process has been identified to have a much higher frequency due to a modal interaction. The modal interaction appears to involve disturbances, excited by second mode and crossflow, being supported by developing stationary crossflow vortices. Comparison with experiments show excellent agreement with the pressure PSD signal measured on the wall. This suggests the dominant mode identified using the STDMD approach is contributing the most to nonlinear disturbance growth, and therefore initiates breakdown.

The current work does not include the global amplification of dynamic modes. Future work will seek to further quantify the amplification associated with instability modes. Nevertheless, this paper demonstrates that the consistent computational and modal methodologies are able to identify physically relevant modes in the presence of breakdown without making the prior assumption as to where transition onset begins. Therefore, this work represents another step towards understanding the underlying flow physics contributing to breakdown on the BoLT shape after undergoing natural transition, and improving prediction of transition in a complex flowfield where assumptions used by traditional stability analyses are no longer valid.

Appendix

A. Isosurface of Streamwise Velocity Perturbations

Similar to Knutson et al. [4], multiple distinct instabilities are observed such as the development of helical perturbations near the centerline due to the lifted boundary layer. Further outboard, helical perturbations develop in the region of interest where rollup is caused by the disturbances interacting with crossflow vortices. On both sides, oblique perturbations develop similar to what was observed by Knutson et al. [4] on BoLT using the stochastic momentum forcing approach. For this case, the isosurface varies in the spanwise direction and oblique structures have varying wave angles. Though it is not shown for the given isosurface level, there are two streaks containing perturbations that are normal to streamwise velocity and are observed when looking at instantaneous pressure perturbations on the surface in [17] and extend to the end of the geometry.

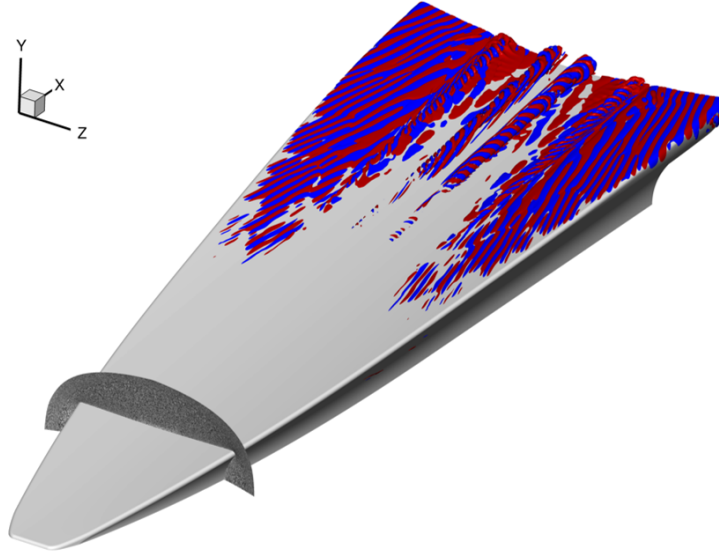


Fig. 13 Isosurface of streamwise velocity perturbations: $u'/u_\infty = \pm 1.0 \times 10^{-3}$ with red as positive and blue as negative. Upper surface is shown only. The forcing level is $P_{RMS} = 0.05\%$ and the computational plane is located at $x/L = 0.23$

B. Data Collection and Sampling

For the current work, it is not trivial to collect time-series data provided the complex geometry and grid. In order to simplify parsing data, slice data was collected by collecting cell centered data from cells that intersect a plane at a specified x-coordinate. In order to extract pertinent flow processes using DMD, the sampling rate has to be sufficiently high frequency to resolve and capture spatio-temporal information. Schmid [45] expresses that a sampling frequency of about three times the Nyquist cutoff ensures satisfactory results from DMD based on past experience. Since the current grid is estimated to resolve up to 500kHz in the streamwise direction based on planar wave propagation, the sampling frequency is 3.3MHz or over three times the Nyquist cutoff of a 500kHz wave. At each streamwise location, the snapshot sequence spans $200 \mu s$ corresponding to one period of a 5kHz wave. This provides 668 snapshots in time with a snapshot spacing of $0.3 \mu s$. The sampling parameters are summarized in the Table 3.

Table 3 Sampling Parameters

Simulation Timestep	20 ns
Number of Snapshots	668
Snapshot Spacing	$0.3 \mu s$
Sampling Frequency	3.3 MHz
Snapshot Sequence	$200 \mu s$
Single Period Wave	5 kHz

Acknowledgments

This work was supported by the DoD HPCMP Hypersonic Vehicle Simulation Institute, the Collaborative Center for Aerospace Sciences, and the Air Force Office of Scientific Research (AFOSR) under award number FA9550-21-1-0106. The views and conclusions contained herein are those of the authors and should not be interpreted as necessarily representing the official policies or endorsements, either expressed or implied, of the AFOSR or the U.S Government. Also, the authors would like to thank Heather Kostak for sharing experimental findings and providing experimental data obtained in the Mach 6 Quiet Tunnel at Texas A&M University.

References

- [1] Johnson, H., Alba, C., Candler, G., MacLean, M., Wadhams, T., and Holden, M., "Boundary-Layer Stability Analysis of the Hypersonic International Flight Research Transition Experiments," *Journal of Spacecraft and Rockets*, Vol. 45, No. 2, 2008, pp. 228, 236. <https://doi.org/10.2514/1.31878>.
- [2] Marineau, E. C., "Prediction Methodology for Second-Mode Dominated Boundary-Layer Transition in Wind Tunnels," *AIAA Journal*, Vol. 55, No. 2, 2017, pp. 484, 499. <https://doi.org/10.2515/1.J055061>.
- [3] Thome, J., Dwivedi, D., Anubhav, Nichols, J. W., and Candler, G. V., "Direct numerical simulation of BoLT hypersonic flight vehicle," *2018 Fluid Dynamics Conference*, 2018, p. 2894.
- [4] Knutson, A. L., Thome, J. S., and Candler, G. V., "Numerical Simulation of Instabilities in the Boundary-Layer Transition Experiment Flowfield," *Journal of Spacecraft and Rockets*, 2020, pp. 1–10.
- [5] Kostak, H. E., Bowersox, R. D., McKiernan, G. R., Thome, J., Candler, G. V., and King, R. A., "Freestream Disturbance Effects on Boundary Layer Instability and Transition on the AFOSR BOLT Geometry," *AIAA Paper*, 2019.
- [6] Kostak, H. E., and Bowersox, R. D. W., "Hypersonic boundary layer off-body and surface measurements on the AFOSR BoLT geometry," *AIAA Paper*, 2020, pp. 2020–1043.
- [7] Li, F., Choudhari, M., and Paredes, P., "Transition Analysis for Isolated Trips on BOLT-II Wind Tunnel and Flight Configurations," *AIAA AVIATION Forum*, 2021.
- [8] Mack, L. M., "Boundary-layer stability theory," *Annu. Rev.*, Vol. 43, 1969, pp. 900–227.
- [9] Fedorov, A., "Transition and stability of high-speed boundary layers," *Annual Review of Fluid Mechanics*, Vol. 43, 2011, pp. 79–95.
- [10] Li, F., Choudhari, M., Chang, C.-L., and White, J., "Secondary Instability of Second Mode Disturbances in Hypersonic Boundary Layers," *RTO AVT-200 RSM-030 Specialists' Meeting on Hypersonic Laminar-Turbulent Transition*, 2012.
- [11] Dinzl, D. J., and Candler, G. V., "Direct simulation of hypersonic crossflow instability on an elliptic cone," *AIAA Journal*, Vol. 55, 2017, pp. 1769–1782.
- [12] Gronvall, J. E., Johnson, H. B., and Candler, G. V., "Hypersonic three-dimensional boundary layer transition on a cone at angle of attack," *AIAA Paper*, Vol. 3561, 2011.
- [13] Choudhari, M., Li, F., and Paredes, P., "Nonlinear Evolution and Breakdown of Azimuthally Compact Crossflow Vortex Pattern over a Yawed Cone," *AIAA Paper*, 2018.
- [14] Taira, K., Brunton, S. L., Dawson, S. T., Rowley, C. W., Colonius, T., McKeon, B. J., Schmidt, O. T., Gordeyev, S., Theofilis, V., and Ukeiley, L. S., "Modal Analysis of Fluid Flows: An Overview," *AIAA Journal*, Vol. 55, No. 12, 2017, pp. 4013, 4041.
- [15] Taira, K., Hemati, M. S., Brunton, S. L., Sun, Y., Duraisamy, K., Bagheri, S., Dawson, S., and Yeh, C., "Modal Analysis of Fluid Flows: Applications and Outlook," *AIAA Journal*, Vol. 58, No. 3, 2020, pp. 998, 1022.
- [16] Jovanovic, M. R., Schmid, P. J., and Nichols, J. W., "Sparsity-Promoting Dynamic Mode Decomposition," *Physics of Fluids*, Vol. 26, No. 2, 2014.
- [17] Johnston, Z. M., and Candler, G. V., "Hypersonic simulation of the BoLT-2 subscale geometry," *AIAA Paper*, Vol. 0366, 2021.
- [18] Mullen, D., and Reed, H. L., "Analysis of the BOLT II - Holden Mission Flight and Wind Tunnel Geometries," *AIAA Paper 2021-0852*, 2021.
- [19] McKenzie, J. F., and Westphal, K. O., "Interaction of Linear Waves with Oblique Shock Waves," *The Physics of Fluids*, Vol. 11, No. 11, 1968, pp. 2350–2362.
- [20] Hader, C., and Fasel, H., "Towards simulating natural transition in hypersonic boundary layers via random inflow disturbances," *J. Fluid Mech.*, Vol. 847, 2018, pp. 2018–386.
- [21] Subbareddy, P. K., and Candler, G. V., "A fully discrete, kinetic energy consistent finite-volume scheme for compressible flows," *Journal of Computational Physics*, Vol. 228, No. 5, 2009, pp. 1347–1364.
- [22] Candler, G. V., Barnhardt, M. D., Drayna, T. W., Nompelis, I., Peterson, D. M., and Subbareddy, P., "Unstructured grid approaches for accurate aeroheating simulations," *AIAA paper*, Vol. 3959, 2007, p. 2007.

- [23] Subbareddy, P. K., Bartkowicz, M. D., and Candler, G. V., "Direct numerical simulation of high-speed transition due to an isolated roughness element," *J. Fluid Mech.*, 2014, pp. 848–878.
- [24] MacCormack, R. W., and Candler, G. V., "The solution of the Navier-Stokes equations using Gauss-Seidel line relaxation," *Computers and fluids*, Vol. 17, No. 1, 1989, pp. 135–150.
- [25] Nompelis, I., "Computational study of hypersonic double-cone experiments for code validation," Ph.D. thesis, University of Minnesota, 2004.
- [26] Larsson, J., Bermejo-Moreno, J., Bodart, J., and Vicquelin, R., "Predicting the operability limit of the HyShot II scramjet using LES," *Center of Turbulence Research Annual Research Briefs*, 2012, pp. 241–251.
- [27] Wright, M. J., Candler, G. V., and Bose, D., "Data-parallel line relaxation method for the Navier-Stokes equations," *AIAA Journal*, Vol. 36, No. 9, 1998, pp. 1603–1609.
- [28] Knutson, A., "Numerical simulation of instabilities in three-dimensional hypervelocity boundary layers," Ph.D. thesis, University of Minnesota, 2020.
- [29] Stetson, K. F., "Hypersonic Boundary-Layer Transition," *Advances in Hypersonics*, 1992, pp. 324–417.
- [30] Huntley, M. B., "Transition on Elliptic Cones at Mach 8," Ph.D. thesis, Princeton University, 2000.
- [31] Smits, A. J., and Dussauge, J.-P., "Turbulent Shear Layers in Supersonic Flow," *Springer, New York*, 2006.
- [32] Thome, J., Knutson, A., and Candler, G. V., "Boundary layer instabilities on BoLT subscale geometry," *AIAA Paper*, 2019, p. 0092.
- [33] Hunt, J. C. R., Wray, A. A., and Moin, P., "Eddies, Streams, and Convergence Zones in Turbulent Flows," *Center for Turbulence Research Paper CTR-S88*, 1988, pp. 193–208.
- [34] Chong, M. S., Perry, A. E., and Cantwell, B. J., "A general classification of three-dimensional flow fields," *Physics of Fluids A: Fluid Dynamics* 2, 765 (1990); doi: 10.1063/1.857730.
- [35] Chu, B.-T., "On the Energy Transfer to Small Disturbances in Fluid Flow (Part I)," *Acta Mechanica*, Vol. 1, No. 3, 1965.
- [36] Hanifi, A., Schmid, P., and Henningson, D., "Transient growth in compressible boundary layer flow," *Physics of Fluids*, Vol. 8, No. 3, 1996.
- [37] George, K. J., and Sujith, R. I., "On Chu's disturbance energy," *Journal of Sound and Vibration*, Vol. 330, 2011.
- [38] Tu, J. H., Rowley, C. W., Luchtenburg, D. M., Brunton, S. L., and Kutz, J. N., "On Dynamic Mode Decomposition: Theory and Applications," *Journal of Computational Dynamics*, Vol. 1, No. 2, 2014, pp. 391–421.
- [39] Hemati, M. S., Williams, M. O., and Rowley, C. W., "Dynamic mode decomposition for large and streaming datasets," *Physics of Fluids* 26, 111701, 2014.
- [40] Hemati, M., Deem, E., Williams, M., Rowley, C., and Cattafesta, L., "Improving Separation Control with Noise-Robust Variants of Dynamic Mode Decomposition," *AIAA Paper 2016-1103*, 2016.
- [41] Hemati, M. S., Rowley, C. W., Deem, E. A., and Cattafesta, L. N., "De-Biasing the Dynamic Mode Decomposition for Applied Koopman Spectral Analysis of Noisy Datasets," *Theoretical and Computational Fluid Dynamics*, Vol. 31, No. 4, 2017, pp. 349, 368.
- [42] DMDTools, <http://z.umn.edu/dmdtools/>, 2015.
- [43] Dwivedi, A., "Global input-output analysis of flow instabilities in high-speed compressible flows," Ph.D. thesis, University of Minnesota, 2020.
- [44] Shrestha, P., and Candler, G., "Direct Numerical Simulation of Trip Induced Transition," *AIAA AVIATION*, 2016.
- [45] Schmid, P., "Dynamic Mode Decomposition of Numerical and Experimental Data," *Journal of Fluid Mechanics*, Vol. 656, 2010.